Topological Electronic Structure and Intrinsic Magnetization in $MnBi_4Te_7$: A Bi_2Te_3 Derivative with a Periodic Mn Sublattice

Raphael C. Vidal,[1,2,*] Alexander Zeugner,[3,*] Jorge I. Facio,[4,*] Rajyavardhan Ray,[4] M. Hossein Haghighi,[4]
Anja U. B. Wolter,[4,2] Laura T. Corredor Bohorquez,[4] Federico Caglieris,[4] Simon Moser,[2,5,6] Tim Figgemeier,[1,2]
Thiago R. F. Peixoto [1,2] Hari Babu Vasili,[7] Manuel Valvidares,[7] Sungwon Jung,[8] Cephise Cacho,[8] Alexey Alfonsov,[4]
Kavita Mehlawat,[4,2] Vladislav Kataev [4] Christian Hess [4,2] Manuel Richter,[4,9] Bernd Büchner,[4,2,10]
Jeroen van den Brink,[4,2,10] Michael Ruck,[3,2,11] Friedrich Reinert,[1,2] Hendrik Bentmann,[1,2,†] and Anna Isaeva [4,2,10,‡]

[1]*Experimental Physics VII, Universität Würzburg, D-97074 Würzburg, Germany*
[2]*Würzburg-Dresden Cluster of Excellence ct.qmat, Germany*
[3]*Faculty of Chemistry and Food Chemistry, Technische Universität Dresden, D-01062 Dresden, Germany*
[4]*Leibniz IFW Dresden, Helmholtzstraße 20, D-01069 Dresden, Germany*
[5]*Experimental Physics IV, Universität Würzburg, D-97074 Würzburg, Germany*
[6]*Advanced Light Source, Lawrence Berkeley National Laboratory, Berkeley, California 94720, USA*
[7]*ALBA Synchrotron Light Source, E-08290 Cerdanyola del Valles, Spain*
[8]*Diamond Light Source, Harwell Campus, Didcot OX11 0DE, United Kingdom*
[9]*Dresden Center for Computational Materials Science (DCMS), Technische Universität Dresden,
D-01062 Dresden, Germany*
[10]*Faculty of Physics, Technische Universität Dresden, D-01062 Dresden, Germany*
[11]*Max Planck Institute for Chemical Physics of Solids, D-01187 Dresden, Germany*

Combinations of nontrivial band topology and long-range magnetic order hold promise for realizations of novel spintronic phenomena, such as the quantum anomalous Hall effect and the topological magnetoelectric effect. Following theoretical advances, material candidates are emerging. Yet, so far a compound that combines a band-inverted electronic structure with an intrinsic net magnetization remains unrealized. $MnBi_2Te_4$ has been established as the first antiferromagnetic topological insulator and constitutes the progenitor of a modular $(Bi_2Te_3)_n(MnBi_2Te_4)$ series. Here, for $n = 1$, we confirm a nonstoichiometric composition proximate to $MnBi_4Te_7$. We establish an antiferromagnetic state below 13 K followed by a state with a net magnetization and ferromagnetic-like hysteresis below 5 K. Angle-resolved photoemission experiments and density-functional calculations reveal a topologically nontrivial surface state on the $MnBi_4Te_7(0001)$ surface, analogous to the nonmagnetic parent compound Bi_2Te_3. Our results establish $MnBi_4Te_7$ as the first band-inverted compound with intrinsic net magnetization providing a versatile platform for the realization of magnetic topological states of matter.

I. INTRODUCTION

Soon after the discovery of topological insulators (TIs) a decade ago [1], the role of magnetism and its potential to modify the electronic topology emerged as a central issue in the field of topological materials. Magnetic degrees of freedom provide a powerful means of tuning the decisive

characteristic of any topological system: its symmetry. By now it is recognized that the interplay between magnetic order and electronic topology offers a rich playground for the realization of exotic topological states of matter, such as the quantum anomalous Hall state [2,3], the axion insulator state [4–6], and magnetic Weyl and nodal-line semimetals [7–11], enabling in turn different routes to spintronic applications [12–14].

The nontrivial topology in paradigmatic TIs like Bi_2Te_3 is a result of band inversion driven by strong spin-orbit interaction [15,16]. Until recently, the interplay with magnetism in topological insulators has been mostly explored by extrinsic methods, such as doping a known TI with magnetic impurities [15] or interfacing it with ferromagnets [17]. Numerous derivatives of Bi_2Te_3 doped by transition metals have been explored over the last

*These authors contributed equally to this work.
†hendrik.bentmann@physik.uni-wuerzburg.de
‡anna.isaeva@tu-dresden.de

years [2,3,18], but the magnetically active atoms did not form a periodic crystal sublattice. Initiated by works on epitaxial $MnBi_2Se_4$ layers [19,20], the compound $MnBi_2Te_4$ has recently arisen as the first derivative of Bi_2Te_3 that hosts structurally and magnetically ordered Mn atoms on well-defined crystallographic sites [21–24]. The emergence of an antiferromagnetic TI state in $MnBi_2Te_4$ is now being broadly scrutinized by theoretical and experimental methods [6,23,25–30]. At the same time, $MnBi_2Te_4$ provides the first example of an intrinsic magnetic TI [23,28,30,31].

In this joint experimental and theoretical work we establish another ternary manganese-bismuth telluride, $MnBi_4Te_7$, i.e., the ($n = 1$) member of a modular $(Bi_2Te_3)_n(MnBi_2Te_4)$ series, as the first instance of a compound that features both an inverted electronic band structure and an intrinsic net magnetization. Moreover, we observe several competing magnetic states in $MnBi_4Te_7$ which, in combination with the presence of topological surface states, could provide a versatile platform for tunability between different topological regimes.

II. CRYSTAL GROWTH AND STRUCTURE

Recent systematic, synthetic explorations of the Mn-Bi-Te system have revealed new compounds that are ordered $(Bi_2Te_3)_n(MnBi_2Te_4)$ ($n = 1, 2$) modular stackings of quintuple (Bi_2Te_3) and septuple $(MnBi_2Te_4)$ blocks [Fig. 1(a)] [30,31]. In this section, we report a new crystal-growth protocol for $n = 1$, assisted by our preceding thermochemical studies [31], and the structure elucidation by single-crystal x-ray diffraction (SCXRD). In Ref. [31] we developed robust synthetic protocols for phase-pure powders of $n = 1$ and $n = 2$ members based on differential scanning calorimetry. For all members of the $(Bi_2Te_3)_n$ $(MnBi_2Te_4)$ ($n = 0, 1, 2$) series we found an ubiquitous deviation from the idealized compositions [24,31]. Henceforward, the title compound is denoted as Mn147, keeping in mind its nonstoichiometry, and the $MnBi_2Te_4$ compound is denoted as Mn124.

As shown first in Ref. [31], Mn147 is thermodynamically stable in a high-temperature interval well above room temperature. Whereas Mn124 melts at 600(5) °C [24], the melting point of Mn147 is 590(5) °C [31] and, thus, offers a very narrow window above the crystallization point of Bi_2Te_3 (586 °C), in which Mn147 can be grown from a melt. Crystal growth is thus very challenging, and our experiments show evidence that polycrystals grown outside the determined temperature window exhibit stacking variants of both Mn124 and Mn147. Mn147 is not thermodynamically stable at room temperature, but can be obtained as a metastable product by quenching from 585 °C [31]. Based on these findings, we have established an optimized crystal-growth technique for Mn147: millimeter-sized platelets [Fig. 1(b)] can be obtained by a stepwise slow cooling of a heterogeneous $MnTe_{(s)}/Bi_2Te_{3(l)}$ melt and long-term
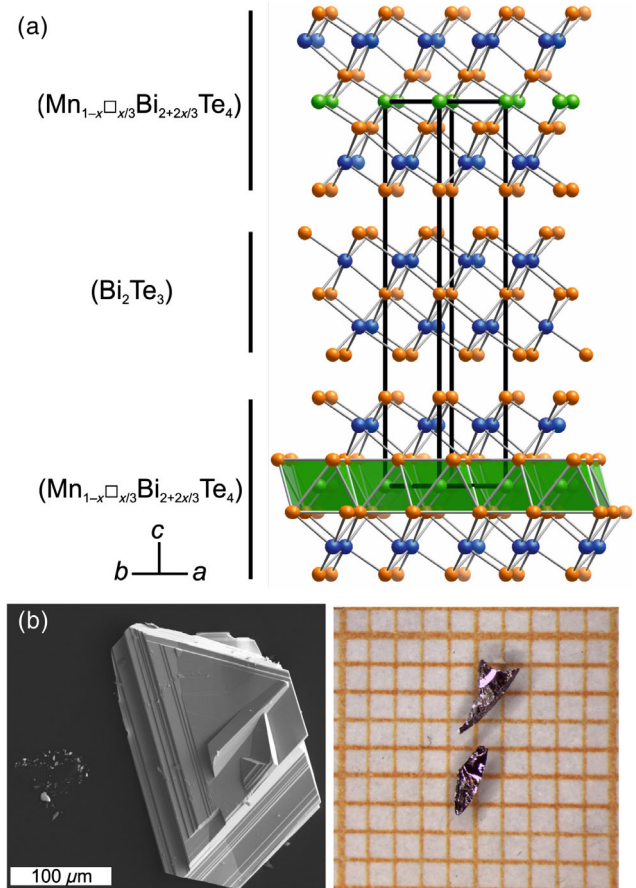

FIG. 1. (a) Crystal structure of $Mn_{1-x}Bi_{4+2x/3}Te_7$ ($GeBi_4Te_7$ structure type) with alternating (Bi_2Te_3) and $(Mn_{1-x}\square_{x/3}Bi_{2+2x/3}Te_4)$ blocks. Mn atoms are shown in green; Bi in blue; Te in orange. (b) As-grown crystals with the experimental composition (EDX) $Mn_{0.8(1)}Bi_{4.3(1)}Te_7$.

annealing at a precisely controlled temperature of 585 °C, followed by rapid water quenching (see the Appendix for further details). These high-quality crystals enable the following studies of the crystal structure, the magnetic order, the transport, and the surface electronic structure (Secs. III and IV). The compositions of all crystals used for physical property measurements are verified by energy-dispersive x-ray spectroscopy (EDX).

Our current structure elucidation by SCXRD confirms cationic nonstoichiometry in Mn147 in full accordance with our previous data on Mn147 powders [31]. The disorder manifests itself in Mn^{2+}/Bi^{3+} antisite defects and related cationic vacancies ($\square$) in the septuple $(Mn_{1-x}\square_{x/3}Bi_{2+2x/3}Te_4)$ blocks, predominantly in the $1a$ site in the middle of the septuple block (Supplemental Material, Tables S1, S2, Note 1 [32]). Interestingly, the (Bi_2Te_3) block appears unaffected by cationic intermixing (Table S3). These mixed occupancies of the cationic positions and Mn vacancies result in a nonstoichiometric composition $Mn_{0.75(3)}Bi_{4.17(3)}Te_7$ as refined from a SCXRD experiment. This stoichiometry slightly deviates

from the one previously determined for polycrystalline powders, $Mn_{0.85(3)}Bi_{4.10(2)}Te_7$ [31]; thus, indicating that a homogeneity range $0.15 \leq x \leq 0.25$ may exist for the $Mn_{1-x}\square_{x/3}Bi_{4+2x/3}Te_7$ phase.

The cationic disorder, however, does not alter the trigonal lattice symmetry of Mn147 (space group $P\bar{3}m1$; the $GeBi_4Te_7$ structure type [33]), neither inhibits long-range magnetic order. A similar intrinsic phenomenon has been reported for isostructural [33], and structurally [24] and compositionally related [34,35] compounds. In contrast to some of them, we find no indications of massive stacking faults in our crystals by x-ray or electron diffraction methods [31].

III. MAGNETIC PROPERTIES

In this section, we analyze the bulk and surface magnetic properties of Mn147 crystals, based on which we discuss the topological electronic properties in Sec. IV. Electrical

resistivity (ρ_{xx}) measurements as a function of temperature (T) reveal a metallic behavior [see Fig. 2(a)]. Focusing on the most salient features of the data, a clear upturn anomaly is visible at 13 K, which is reminiscent of the typical signature of magnetic ordering in itinerant materials [36]. The upturn indicates enhanced fluctuations causing electron scattering, which is strongly reduced in the ordered phase, in which a steep decrease of ρ_{xx} occurs. Upon lowering the temperature, a jumplike drop at about 5 K reveals further reduction of scattering, possibly related to a rearrangement of the magnetic structure.

Indeed, measurements of the magnetization (M) in an external field (H) on a $Mn_{0.82(7)}Bi_{4.2(1)}Te_{7.00(5)}$ crystal (as determined by EDX) as a function of temperature show an antiferromagnetic phase transition at $T_N = 13$ K [Fig. 2(b)]. For $H \perp ab$ and small fields, such as $H = 200$ Oe, a ferromagnetic-like increase occurs upon further cooling. This is followed by a splitting of field-cooled (FC) and zero field-cooled (ZFC) curves at around 7 K, as well as a kink
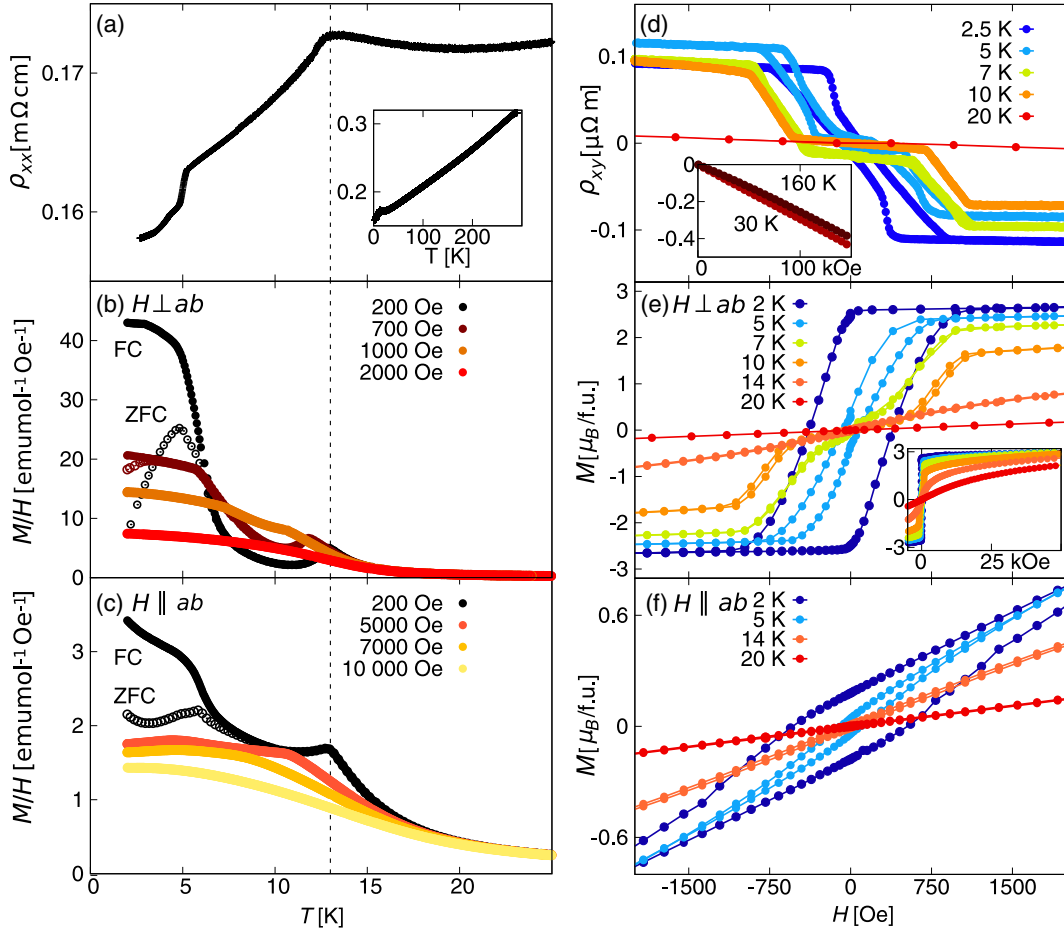

FIG. 2. Magnetic and transport properties of Mn147. (a) In-plane electrical resistivity as a function of the temperature. (b),(c) Normalized magnetization as a function of temperature for fields applied both perpendicular and parallel to the *ab* directions. Open and filled symbols correspond to ZFC and FC protocols, respectively. (d),(e) Hall resistivity and magnetization as a function of the field applied perpendicular to the *ab* planes. (f) Magnetization as a function of the field applied parallel to the *ab* planes. The hysteretic behavior for temperatures $T \leq 5$ K indicates ferromagnetic (intraplane) interactions.
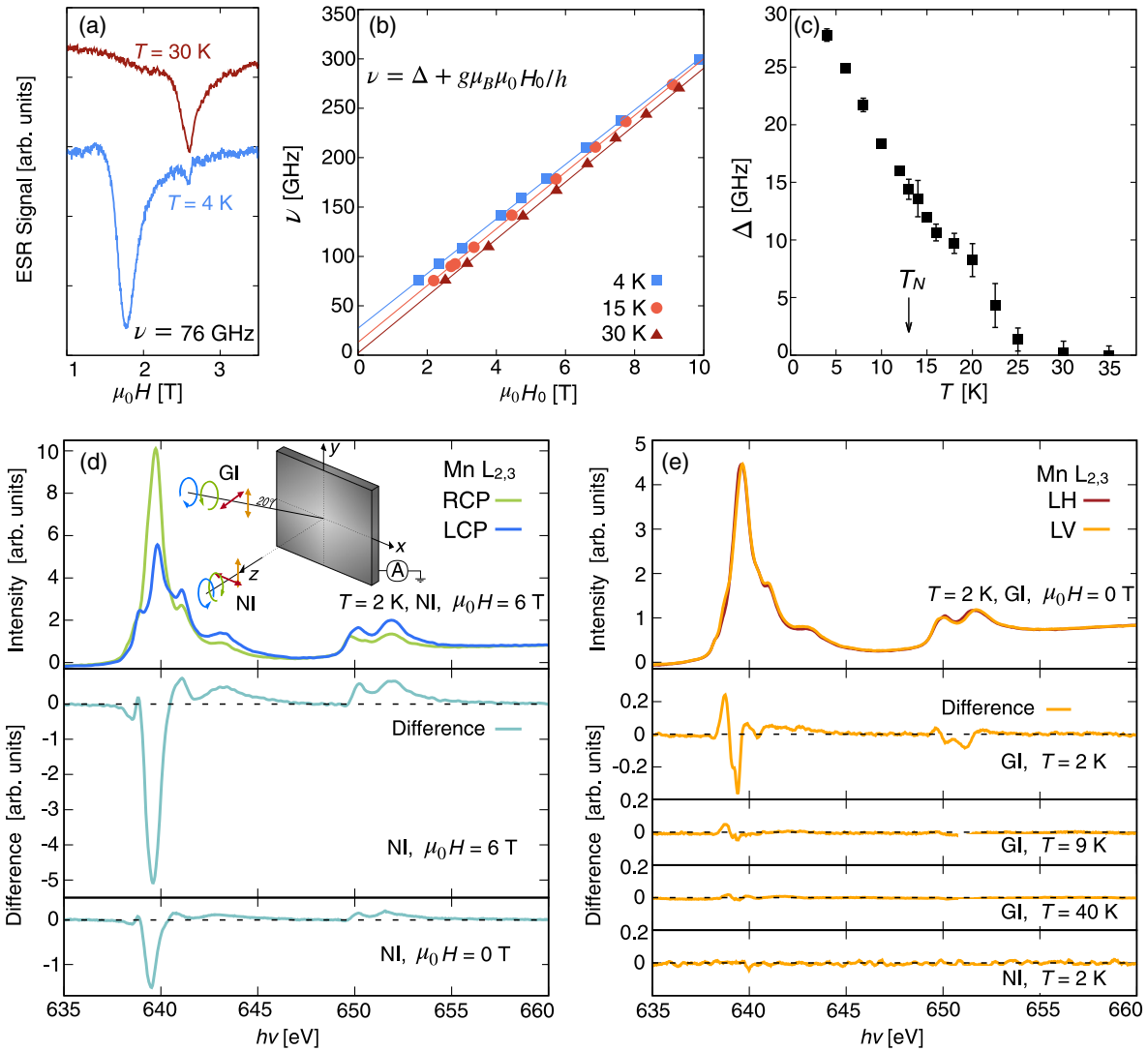
FIG. 3.   Spectroscopy of magnetic properties in Mn147. (a) Typical ESR spectra measured at $T = 4$ K and $T = 30$ K. (b) Frequency dependence of the resonance field of the ESR signal measured at temperatures of 4, 15, and 30 K. (c) The anisotropy gap Δ as a function of temperature extracted from (a) by fitting $\nu = \Delta + g\mu_B\mu_0 H_0/h$. (d) XMCD and (e) XMLD data for Mn147(0001) obtained at the Mn $L_{2,3}$ absorption edge with circularly polarized (RCP and LCP) and linearly polarized (LV and LH) light, respectively. Measurements are performed in normal (NI) and grazing (GI) light incidence geometries, as sketched in the inset of (d). XMCD signals are shown for an external field ($\mu_0 H = 6$ T) along the light incidence direction and for remnant conditions ($\mu_0 H = 0$ T) at $T = 2$ K. (e) XMLD data without external field are reported for different temperatures.

and a peak at about 5 K, respectively, the latter coinciding with the jump in the resistivity. Both features are rapidly suppressed by applying an external magnetic field.

In the magnetically ordered phase, interesting metamagnetic behavior occurs for $H \perp ab$ as is evidenced by the magnetization curves [Fig. 2(e)]. For example, at $T = 10$ K a spin-flop-like feature is observed, and for $T < 7$ K dominating hysteresis typical for ferromagnets is apparent. This complex magnetic phenomenology is also reproduced by the Hall resistivity ρ_{xy} [Fig. 2(d)]. For $T < T_N$, the system exhibits an anomalous Hall effect tracking the observed metamagnetic behavior. For $T \leq 7$ K the data reveal an additional metamagnetic transition in the

low-field region $\mu_0 H \leq 300$ Oe. This observation is confirmed by a close inspection of the magnetization data. At 2.5 K a large hysteresis associated with global ferromagnetism is present. Above T_N the anomalous contribution disappears, and only a standard component persists with a negative sign consistent with an *n*-type conduction [inset in Fig. 2(d)].

The magnetic anisotropy of the compound is examined via additional measurements for $H \parallel ab$ [Figs. 2(c) and 2(f)]. The magnetic moment values in the ordered state are much lower in this case. At lower fields both an antiferromagnetic transition and a ZFC-FC splitting are observed, but the suppression of these features occurs at higher fields than

for $H \perp ab$. For the $H \| ab$ direction just below T_N the magnetization increases almost linearly with the applied magnetic field as expected for an antiferromagnet. On top of that, a spin reorientation at lower temperatures is indicated by an increase of M/H below ca. 10 K and a ferromagnetic net magnetization is clearly present. Apparently, the field necessary to observe such a feature can be sample dependent, as is evident from a comparison of our results with recent reports [37–39]. This finding may be associated with slight differences in the Mn content due to Mn/Bi intermixing and Mn vacancies, which, however, have no influence on the lattice symmetry. Notably, all reports are in line regarding the behavior of magnetization as a function of the magnetic field in both directions. The results show that the system is yet not fully saturated at $\mu_0 H = 5$ T as indicated by a small slope at higher fields [inset in Fig. 2(e)]. High-field experiments are necessary to gain a better insight into the details of the magnetic phase diagram.

The Curie-Weiss fitting of the magnetization high-temperature data in both directions yields positive values of the Curie-Weiss temperature: $\theta_{CW}^{ab} = 13.7(5)$ K and $\theta_{CW}^c = 14.7(5)$ K, thus, confirming the predominantly ferromagnetic character of the largest (intraplane) exchange interaction (see Supplemental Material, Note 2 and Fig. S1 [32]). In addition, the estimated effective magnetic moments, given the homogeneity range ($0.15 \leq x \leq 0.25$), fall into the ranges $5.2\mu_B \leq \mu_{eff}^{ab} \leq 5.6\mu_B$ and $5.1\mu_B \leq \mu_{eff}^c \leq 5.5\mu_B$, where μ_B is the Bohr magneton, which suggest the manganese(II) high-spin configuration $S = \frac{5}{2}$. The microscopic nature of the different magnetic states as a function of field and temperature is a matter of debate and requires further elucidation.

The observed high-frequency electron spin resonance (ESR) signal of Mn147 [Figs. 3(a)–3(c)] is almost isotropic above $T \sim 30$ K and follows a typical Mn(II)-ion paramagnetic resonance condition $h\nu = g\mu_B \mu_0 H_0 |m_s^z - (m_s^z \pm 1)|$ with the g factor very close to 2. Here, h is the Planck constant, and m_s^z is the projection of the spin on the quantization (magnetic field) axis. Importantly, below $T \sim 30$ K an energy gap Δ develops in the ESR response, and the resonance condition is modified to $\nu = \Delta + g\mu_B\mu_0 H_0/h$. The measured linear dependence of ν vs $\mu_0 H_0$ for $\mu_0 H \| ab$ [Fig. 3(a)] is typical for the wave vector $q = 0$ spin wave excitation (ferromagnetic resonance—FMR) in an easy-axis-type ferromagnetically ordered material, where Δ represents the magnetic anisotropy gap. Considering the smallness of Δ as compared with the applied magnetic fields, such linearity is incompatible with the resonance response of an ordered collinear antiferromagnet in this field regime [40,41]. The opening of the excitation gap Δ at $T \leq 30$ K and its gradual increase [Fig. 3(b)] shows evidence of significant ferromagnetic spin correlations on the time scale of ESR (10^{-11} s) unrelated to 3D antiferromagnetic ordering which sets in at $T_N = 13$ K. Therefore, given the pronounced low

dimensionality of the system, it is likely that the Mn-containing blocks are inherently ferromagnetic and give rise to a typical FMR signal in strong fields. At the same time, the application of a magnetic field suppresses the expected much weaker interlayer antiferromagnetic coupling responsible for the 3D long-range order at T_N in zero and small fields, whereas a paramagnetic state with strong intraplane ferromagnetic correlations—denoted in the following as correlated paramagnet (CPM)—persists up to temperatures of the order 30 K.

To complement the magnetic characterization, we carried out x-ray magnetic circular (XMCD) and linear dichroism (XMLD) experiments at the Mn $L_{2,3}$ absorption edge in total electron yield mode (TEY) with a typical probing depth of a few nm [42]. The XMCD data collected at $T = 2$ K provide evidence for a substantial remanent net magnetization of the Mn ions along the surface normal [Fig. 3(d)], in sharp contrast to our previous observations for Mn124 with antiferromagnetic order [24]. This confirms that the spontaneous ferromagnetic polarization observed in the bulk magnetization data below $T \sim 5$ K extends up to the surface layers. A sizable XMLD signal in grazing light incidence and its absence in normal incidence further confirm the remnant out-of-plane magnetization [Fig. 3(e)] in agreement with the ESR results. The XMLD signal gradually diminishes with increasing temperature, confirming its magnetic origin and indicating the transition into the paramagnetic regime, in line with our bulk magnetization results.

By density-functional calculations (DFT) we consider various possible magnetic structures for the ordered MnBi$_4$Te$_7$ model (see Supplemental Material, Note 3 [32]). The Mn atoms are found in the high-spin Mn(II) configuration, in agreement with the high-temperature magnetization measurements and similar to Mn124 [24]. Our calculations show that the magnetic moments within the Mn layers prefer intraplane ferromagnetic order with an out-of-plane spin configuration. The first-neighbor coupling is estimated as -0.09 meV/μ_B^2, which is very close to the value reported for Mn124 [23]. Furthermore, we find that antiferromagnetic ordering between the Mn layers (AFM1 state) results in a smaller total energy than the ferromagnetic ordering (FM state). The energy difference is, however, only about 0.5 meV/Mn atom, which is an order of magnitude smaller than in Mn124 [22]. Moreover, this value is very close to the magnetic anisotropy energy, which yields about 0.5 meV/Mn atom in favor of the easy-axis configuration. These estimates corroborate a scenario with competing magnetic states differing slightly in energy, and, hence, a more complex magnetic response shown by Mn147, as compared to Mn124.

IV. ELECTRONIC STRUCTURE AND TOPOLOGICAL SURFACE STATE

Having established the crystal structure and the magnetic properties of Mn147, we will now discuss its electronic

structure based on DFT and angle-resolved photoemission (ARPES) experiments. The structural resemblance between Mn147 and Bi_2Te_3 opens the question, to what extent Mn147 inherits properties from the (Bi_2Te_3) building blocks. We begin our theoretical analysis of the topology of the electronic structure with an auxiliary calculation without spin polarization (see Supplemental Material, Note 4 [32]), which shows that, in the absence of magnetism, the system would be both a strong topological insulator and a topological crystalline insulator, just like Bi_2Te_3 [43].

The influence of magnetism on the topological properties is first examined for the band-inversion phenomena. Figures 4(a) and 4(b) show the band structure of Mn147 for the FM and AFM1 (layerwise AFM) order, respectively (see Fig. S3 [32]). The symbol size is proportional to the overlap between the corresponding Bloch states and the indicated orbitals. For reference, Fig. S3f shows the well-known case of Bi_2Te_3, whose nontrivial topology

originates in the inversion between Bi p_z and Te p_z orbitals of opposite parity [15,16,32]. The same orbitals contribute to the band inversion in Mn147 with the difference that the inverted bands are spin-polarized in the presence of a ferromagnetic component. Namely, the occupied Bi states form two bands [$B1$ and $B3$ in Fig. 4(a)] of predominantly opposite spin.

Naturally, in the AFM1 configuration the spin polarization in each band is compensated, i.e., each band is spin degenerate. In this phase, the system realizes a Z_2 antiferromagnetic topological insulator (AFMTI), protected by a combination of time-reversal symmetry and translation along the c axis. This case is analogous to the recently established AFMTI state in Mn124 [23]. The Z_2 topology is analyzed in Fig. 4(c) based on a Wannier charge center (WCC) in the $k_z = 0$ plane. An arbitrary horizontal line crosses the WCC an odd number of times, and thus the $k_z = 0$ plane behaves as a quantum spin Hall insulator [44]. This ensures the existence of gapless surface states on side surfaces parallel to the c axis.

A natural question is to what extent the observed structure tendencies to Mn/Bi intermixing and to Mn vacancies affect the electronic structure. To address this point, we performed supercell calculations for the compositions $Mn_{0.75}Bi_{4.25}Te_7$ and $Mn_{0.50}\square_{0.25}Bi_{4.25}Te_7$ (lifting up the restriction of electron neutrality used in the SCXRD refinements). Our calculations show that the fundamental gap remains open, suggesting that, in the present amounts, Mn/Bi intermixing and Mn vacancies do not affect the nontrivial topology of the material, but rather only shift the chemical potential (see Supplemental Material, Note 7 [32]).

The existence of a topologically nontrivial surface state is confirmed by the calculated (0001) surface spectral density in Fig. 4(d) for a quintuple-layer (QL) termination. As expected for the AFM1 state with an intraplane ferromagnetic configuration the surface spectral density shows a gaplike feature at the $\bar{\Gamma}$ point [23]. We find a similar situation in our surface calculations for the case of a septuple-layer (SL) termination (Fig. S8) and also for a FM magnetic configuration (Fig. S5).

To experimentally support the nontrivial topology of the electronic structure predicted by our calculations, we conducted ARPES measurements on the natural cleaving (0001) surface of Mn147 (Fig. 5). The overview band structures [Fig. 5(a), Supplemental Material Figs. S9d, S9e, Note 6 [32]] bear clear resemblance to previous ARPES experiments for the topological insulator Bi_2Te_3 [15,45]. Most importantly, we likewise find a state with a V-shaped dispersion in the bulk gap between the conduction and valence band states (BCB and BVB), near the Fermi level E_F [Figs. 5(b) and 5(g)]. Systematic photon-energy-dependent measurements confirm the surface character of this state [Fig. 5(d)]. By comparison to our density-functional calculations in Fig. 4(d) we identify it as a topologically nontrivial surface state (TSS).
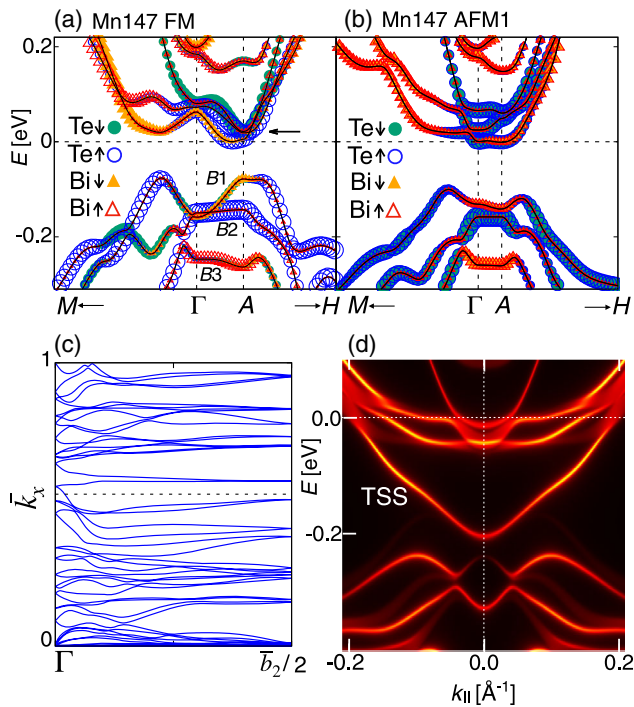

FIG. 4. Band inversion phenomena in Mn147 (GGA + U + SOC). (a) Band structure in the ferromagnetic configuration. The symbol size in each k point and band is proportional to the overlap between the corresponding Bloch state and the Te and Bi p orbitals, respectively, depicted in different colors. Filled (empty) dots correspond to spin-down (spin-up). The black arrow indicates the energy of the Weyl node of lowest energy in the conduction band. (b) Band structure for the antiferromagnetic AFM1 configuration. (c) Wannier center evolution in the $k_z = 0$ plane. k_x is the crystal momentum along the primitive lattice vector $\bar{b}_1$ and $\bar{b}_2$ is the second primitive vector in the $k_z = 0$ plane. (d) Mn147(0001) surface spectral density along the $\bar{\Gamma}$-$\bar{M}$ direction for a quintuple layer termination.
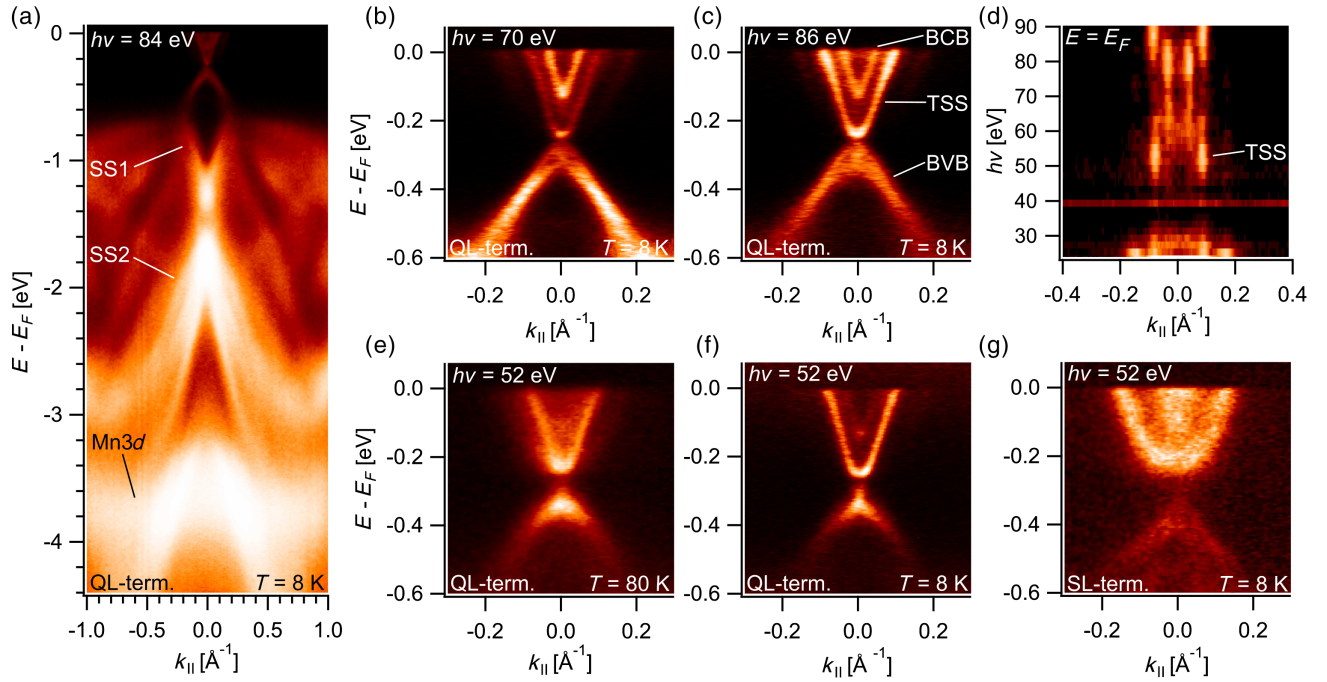
FIG. 5. Electronic structure of the Mn147(0001) surface as measured by ARPES. (a) Overview data set of the valence band structure obtained at $T = 8$ K showing characteristic surface states SS1 and SS2 and a feature related to Mn $3d$ states (cf. Figs. S9–S12 [32]). (b),(c),(f) High-resolution data sets of the electronic structure near E_F obtained at different photon energies and a temperature of $T = 8$ K, showing a topological surface state (TSS) in the gap between conduction and valence-band derived states (BCB and BVB). (d) Photon-energy dependence of the ARPES intensity at E_F ($T = 8$ K). (e) Same as in (f), but for $T = 80$ K. (g) Same as in (f), but for a septuple layer (SL) termination. All other data sets in Fig. 4 are assigned to a quintuple layer (QL) termination. The ARPES data sets in Fig. 5 are measured along the $\bar{\Gamma}$-$\bar{M}$ high-symmetry direction.

The observation of conduction band states below E_F is in line with our transport measurements, although the prominent feature BCB shows a markedly 2D character and possibly arises from band bending, as commonly found for Bi_2Te_3 [46] and Bi_2Se_3 [47]. At higher binding energies in the valence band, we observe additional surface states SS1 and SS2 [Fig. 5(a), Figs. S9d, S9e] that are similar to those previously detected for Bi_2Te_3 [45]. These states are highly surface localized well within a single (Bi_2Te_3) QL [45], suggesting that our results in Figs. 5(a)–4(f) represent a surface terminated by a Bi_2Te_3 QL. This is supported by our calculations in Fig. S7a [32] for Bi_2Te_3-terminated Mn147, where similar surface states are found. Measurements on a single (0001) surface also revealed areas with a different well-defined band structure [Fig. 5(g), Fig. S10], which we tentatively attribute to the second possible surface termination by a ($MnBi_2Te_4$) SL. The reduced data quality for this SL termination may arise from the higher defect density in the SL than in the QL as evidenced by our x-ray diffraction results in Sec. II. Nevertheless, we observe qualitatively similar features in ARPES as for the QL termination. Both terminations accommodate a dispersionless feature at a binding energy near 3.8 eV, which can be attributed to the Mn $3d$ states [Fig. 5(a); Supplemental Material Fig. S10], as confirmed by resonant photoemission measurements at the Mn L edge (Fig. S11).

Unlike for Bi_2Te_3, our measurements for Mn147 in the AFM1 state suggest the presence of a finite separation between the TSS and the BVB. This gaplike feature shows a subtle photon-energy dependence arising mainly from changes in the spectral appearance of the BVB maximum, as exemplified by the three data sets in Figs. 5(b), 5(c), and 5(f). The latter consists of at least two different features within a narrow energy range that exhibit complex $h\nu$-dependent intensity variations and possibly arise from a coexistence of surface- and bulk-derived states. Measurements at T = 80 K [Fig. 5(e)] do not show strong changes in the spectra for $h\nu = 52$ eV. However, towards higher temperatures we observe an increased spectral-weight filling of the gaplike feature, suggesting its mitigation with increasing temperature (Fig. S12).

A comprehensive picture of the detailed spectral-weight behavior of the TSS near the Dirac point is yet to emerge. Gaplike features, even in the paramagnetic regime, are also found in different magnetically doped TIs [48,49], in Mn124 [23,25] and, very recently, also in Mn147 [37,39,50,51]. We expect our detailed discussion of the $h\nu$ dependency to be a useful ingredient, which, e.g., indicates a gaplike feature considerably smaller than the one observed in [37]. Additionally, other reports have found a vanishing gap in Mn147 [52–54] and argued about a surface magnetic structure possibly different from that in

the bulk. At low temperatures, our XMCD measurements provide evidence for a finite net magnetization at the surface, which motivates future ARPES measurements in this temperature regime. These developments show that, likely, additional spectroscopic experiments, e.g., including spin resolution, scanning tunneling microscopy, and transport experiments on thin flakes will help to further elucidate this essential point.

V. MAGNETIC TOPOLOGICAL PHASES

Motivated by the experimental observations of a TSS due to band inversion and of the competition between different magnetic phases, we outline, based on our calculations, a topological phase diagram as a function of temperature and magnetic field. Figure 6 sketches the phases theoretically explored in the ordered $MnBi_4Te_7$ model. Below the Neél temperature, our calculations predict that the antiferromagnetic phase (AFM1) hosts a Z_2 topological insulating phase protected by a combination of the time-reversal and translation symmetries along the polar axis. In the lowest-temperature regime the experiments reveal a phase with net magnetization at zero magnetic field [see Figs. 2(e) and 2(f)]. To mimic this regime we consider a collinear FM state which, interestingly, also features a nontrivial topology (see Supplemental Material, Note 5 [32]). Namely, this phase realizes a topological crystalline insulator (TCI) tunable by the magnetization orientation. Specifically, the crystal structure presents three mirror planes that contain the polar axis and are related by $2\pi/3$ rotations. When the magnetization points perpendicular to one of these planes, it preserves the corresponding reflection symmetry. The calculated mirror Chern number in such a magnetic configuration equals -1. For other magnetization orientations, as in particular out-of-plane orientations, the topological protection at
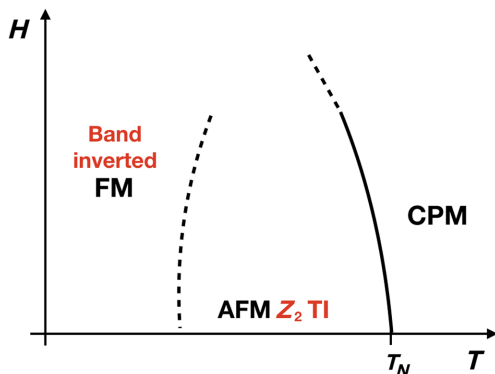

FIG. 6.　Schematic topological phase diagram of $MnBi_4Te_7$. The scheme follows the experimentally observed trends: a correlated paramagnetic state above T_N, followed by an antiferromagnetic phase that at lower temperatures evolves to a magnetic state with a strong ferromagnetic component. The text in red highlights possible nontrivial topology (see text for details).

the (0001) surface is lifted and the corresponding surface state is gapped (see Fig. S5 [32]). In addition, as shown in Fig. 4(a), doped samples can be of interest, since a ferromagnetic component splits the double degeneracy of the bulk bands and opens up the possibilities of Weyl physics. Indeed, Weyl nodes are revealed only 24 meV above the gap, very close to the bottom of the conduction bands [see the arrow in Fig. 4(a) and Fig. S6].

VI. CONCLUSION

We present a comprehensive study of structural, magnetic, and electronic properties of the Bi_2Te_3-derivative $Mn_{0.75(3)}Bi_{4.17(3)}Te_7$, i.e., the ($n = 1$)-member Mn147 of the modular $(Bi_2Te_3)_n(MnBi_2Te_4)$ series. Our results indicate that Mn147 realizes an intrinsic magnetic topological insulator, similar to the recently established first antiferromagnetic topological insulator $MnBi_2Te_4$ for $n = 0$ [23]. Unlike for $MnBi_2Te_4$, Mn147 develops a strong out-of-plane ferromagnetic component at low temperatures. In this regime Mn147 realizes the first instance of a compound that features both an *intrinsic* net magnetization and a topologically nontrivial surface state originating from a band inversion. In the thin-film limit these properties could facilitate the realization of the quantum anomalous Hall effect in an intrinsic material, as recently reported for Mn124 where, however, it requires large external fields due to the robust antiferromagnetism [55,56]. Moreover, our calculations show how the complex magnetic phases of Mn147, that we observe experimentally, may facilitate the tunability between different topological regimes, including antiferromagnetic topological and topological crystalline insulator states.

APPENDIX: METHODS

In this appendix we provide further information on the different methods used in this work.

1. Crystal growth

First indications for the existence of $Mn_{1-x}\square_{x/3}Bi_{4+2x/3}Te_7$ ($0.15 \leq x \leq 0.25$) and its composition were obtained in our previously published differential scanning calorimetry experiments [24]. Attempts to synthesize a phase-pure powder of $Mn_{0.85}Bi_{4.10}Te_7$ following the synthetic route described in Ref. [24], namely by long-term annealing of a stoichiometric mixture of Bi_2Te_3 and α-MnTe at subsolidus temperature, lead to considerable amounts (up to 15 wt %) of $MnBi_2Te_4$ admixtures. A phase-pure ingot of $Mn_{0.85}Bi_{4.10}Te_7$ was synthesized by annealing at 590 °C for 3 days, subsequent slow cooling to 585 °C and, finally, annealing for 1 day followed by rapid quenching in water. Worth noting is that powders with the idealized $MnBi_4Te_7$ composition that were prepared by this route contained impurities, suggesting that this composition lies outside the homogeneity range. High-quality single crystals of $Mn_{1-x}\square_{x/3}Bi_{4+2x/3}Te_7$ were grown by slow cooling (-1 K/h) of a melt from 650 °C down to 585 °C (right above the solidification point of Bi_2Te_3), followed by annealing for 10 days and rapid quenching. Platelet like strongly intergrown crystals were mechanically extracted from the obtained ingots. Their compositions were controlled by EDX analysis.

2. X-ray diffraction and energy-dispersive x-ray spectroscopy

Single-crystal x-ray diffraction data were collected on a four-circle Kappa APEX II CCD diffractometer (Bruker) with a graphite(002) monochromator and a CCD detector at $T = 296(1)$ K. Mo-K_α radiation ($\lambda = 71.073$ pm) was used. A numerical absorption correction based on an optimized crystal description was applied [57], and the initial structure solution was performed in JANA2006 [58]. The structure was refined in SHELXL against F_o^2 [59]. For further details on the crystal structure investigations of $Mn_{0.75(3)}Bi_{4.17(3)}Te_7$, see Ref. [60].

Powder x-ray diffraction data were measured using an X-Pert Pro diffractometer (PANalytical) with Bragg-Brentano geometry or a Huber G670 diffractometer with an integrated imaging plate detector and read-out system. Both machines operate with a curved Ge(111) monochromator and Cu-$K_{\alpha1}$ radiation ($\lambda = 154.06$ pm). Variable divergence slits were used on the X-Pert Pro equipment to keep the illuminated sample area constant. The graphics of the structures were developed with the DIAMOND software [61].

Energy dispersive x-ray spectra (EDX) were collected on a scanning electron microscope Hitachi SU8020 using an Oxford Silicon Drift X-MaxN detector at an acceleration voltage of 20 kV and 100 s accumulation time. The EDX analysis was performed using the P/B-ZAF standardless method (where $Z =$ atomic number correction factor, $A =$ absorption correction factor, $F =$ fluorescence factor, and $P/B =$ peak to background model). Experimentally determined compositions (EDX) fall into a range from $Mn_{0.7(1)}Bi_{4.4(1)}Te_7$ to $Mn_{0.8(1)}Bi_{4.3(1)}Te_7$.

3. Angle-resolved photoelectron spectroscopy

ARPES measurements on the (0001) surface of cleaved crystals in a temperature range range between 8 and 80 K were carried out at the high-resolution-branch of beamline i05 at the Diamond Light Source, U.K., using p-polarized photons with energies between $h\nu = 20$ and 90 eV and energy resolution <10 meV [Fig. 5 and S10]. The spot size of the photon beam was ca. 30 μm. Supplementary ARPES experiments were performed at the Microscopic and Electronic Structure Observatory (MAESTRO) at beamline 7 of the Advanced Light Source (ALS) (Fig. S9) and at the LE branch of APE beamline at the Elettra synchrotron (Fig. S11). All measurements were performed in ultrahigh vacuum of lower than 10^{-10} mbar. Supplementary core-level photoemission data were acquired at the ASPHERE III end station at beamline P04 of PETRA III (DESY, Hamburg) (Fig. S11).

4. Electron spin resonance measurements

ESR experiments were performed on a single crystal with a homemade ESR setup in the microwave frequency range $\nu = 75$–300 GHz, in the temperature range $T = 4$–35 K, and in magnetic fields up to $\mu_0H_0 = 16$ T.

5. X-ray magnetic circular and linear dichroism

XMCD and XMLD measurements on the (0001) surface of cleaved crystals were carried out in total electron yield (TEY) mode at the BOREAS beamline of the ALBA synchrotron [62].

6. Density-functional calculations

Fully relativistic density functional theory (DFT) calculations were performed using the Perdew-Burke-Ernzerhof implementation [63] of the generalized gradient approximation (GGA) and treating the spin-orbit coupling in the 4-spinor formalism, as implemented in FPLO-18 [64]. For results presented in the main text, the experimental crystal structure based on a fully ordered $MnBi_4Te_7$ was used in our calculations. Namely, the cationic intermixing and cation deficiency were neglected and the stoichiometric limit $MnBi_4Te_7$ was considered. Effects of these sorts of defects were studied by supercell calculations (see Supplemental Material, Note 7 [32]). For the ordered model calculations, a linear tetrahedron method with a mesh of $16 \times 16 \times 2$ subdivisions (or $16 \times 16 \times 1$ in the AFM1 state) in the full Brillouin zone was used. $GGA + U$ calculations were performed using the atomic limit implementation of the double-counting correction and fixing $J = 1$ eV. The value of U affects the resulting bulk gap and determines at which energies the spectral weight associated with Mn d states is placed. We find that the position of the Mn $3d$ states measured with core-level spectroscopy (see Fig. S11 [32]) is best described by a moderate value of $U \sim 2$ eV (see Fig. S3c [32]). This value renders a bulk gap of ~ 75 meV. In $MnBi_2Te_4$, higher values of U have been used aiming to reproduce the experimental estimation of the gap [23]. The difficulty in finding a single value of U that correctly accounts for all experimental results suggests that a quantitative comparison in these materials may necessitate the usage of exchange and correlation functionals beyond $GGA + U$. The statements on the total energy calculations are, however, robust, as shown in the Supplemental Material, Note 3. For the surface spectral calculations, as well as for the search of Weyl nodes, an accurate tight-binding model was built by constructing Wannier functions with the projection method implemented in the PYFPLO interface of FPLO [64]. The Bi $6p$, Te $5p$, and Mn $3d$ orbitals were considered in this construction. The mirror Chern numbers were computed based on this Hamiltonian as implemented in Ref. [65].

7. Magnetization and transport

The dc magnetization measurements were performed in a superconducting quantum interference device (SQUID) vibrating sample magnetometer (VSM) from Quantum Design for 1.8 K up to room temperature and in magnetic fields up to 7 T. Zero-field-cooled (ZFC) and field-cooled (FC) magnetization curves were recorded upon warming.

The transport properties were performed in the standard four-wire configuration using a homemade probe inserted in a He-bath cryostat by Oxford Instruments, endowed with a 15/17 T magnet.

[1] M. Z. Hasan and C. L. Kane, *Colloquium: Topological Insulators*, Rev. Mod. Phys. **82**, 3045 (2010).

[2] Cui-Zu Chang, Jinsong Zhang, Xiao Feng, Jie Shen, Zuocheng Zhang, Minghua Guo, Kang Li, Yunbo Ou, Pang Wei, Li-Li Wang, Zhong-Qing Ji, Yang Feng, Shuaihua Ji, Xi Chen, Jinfeng Jia, Xi Dai, Zhong Fang, Shou-Cheng Zhang, Ke He, Yayu Wang, Li Lu, Xu-Cun Ma, and Qi-Kun Xue, *Experimental Observation of the Quantum Anomalous Hall Effect in a Magnetic Topological Insulator*, Science **340**, 167 (2013).

[3] Cui-Zu Chang, Weiwei Zhao, Duk Y. Kim, Haijun Zhang, Badih A. Assaf, Don Heiman, Shou-Cheng Zhang, Chaoxing Liu, Moses H. W. Chan, and Jagadeesh S. Moodera, *High-Precision Realization of Robust Quantum Anomalous Hall State in a Hard Ferromagnetic Topological Insulator*, Nat. Mater. **14**, 473 (2015).

[4] D. Xiao, J. Jiang, J. H. Shin, W. Wang, F. Wang, Y. F. Zhao, C. Liu, W. Wu, M. H. W. Chan, N. Samarth, and C. Z. Chang, *Realization of the Axion Insulator State in Quantum Anomalous Hall Sandwich Heterostructures*, Phys. Rev. Lett. **120**, 056801 (2018).

[5] Nicodemos Varnava and David Vanderbilt, *Surfaces of Axion Insulators*, Phys. Rev. B **98**, 245117 (2018).

[6] N. P. Armitage and Liang Wu, *On the Matter of Topological Insulators as Magnetoelectrics*, SciPost Phys. **6**, 46 (2019).

[7] Enke Liu, Yan Sun, Nitesh Kumar, Lukas Muechler, Aili Sun, Lin Jiao, Shuo-Ying Yang, Defa Liu, Aiji Liang, Qiunan Xu, Johannes Kroder, Vicky Süß, Horst Borrmann, Chandra Shekhar, Zhaosheng Wang, Chuanying Xi, Wenhong Wang, Walter Schnelle, Steffen Wirth, Yulin Chen, Sebastian T. B. Goennenwein, and Claudia Felser, *Giant Anomalous Hall Effect in a Ferromagnetic Kagome-Lattice Semimetal*, Nat. Phys. **14**, 1125 (2018).

[8] Kyoo Kim, Junho Seo, Eunwoo Lee, K.-T. Ko, B. S. Kim, Bo Gyu Jang, Jong Mok Ok, Jinwon Lee, Youn Jung Jo, Woun Kang, Ji Hoon Shim, C. Kim, Han Woong Yeom, Byung Il Min, Bohm-Jung Yang, and Jun Sung Kim, *Large Anomalous Hall Current Induced by Topological Nodal Lines in a Ferromagnetic van der Waals Semimetal*, Nat. Mater. **17**, 794 (2018).

[9] Libor Šmejkal, Tomáš Jungwirth, and Jairo Sinova, *Route towards Dirac and Weyl Antiferromagnetic Spintronics*, Phys. Status Solidi RRL **11**, 1700044 (2017).

[10] D. F. Liu, A. J. Liang, E. K. Liu, Q. N. Xu, Y. W. Li, C. Chen, D. Pei, W. J. Shi, S. K. Mo, P. Dudin *et al.*, *Magnetic Weyl Semimetal Phase in a Kagomé Crystal*, Science **365**, 1282 (2019).

[11] Madhav Prasad Ghimire, Jorge I. Facio, Jhih-Shih You, Linda Ye, Joseph G. Checkelsky, Shiang Fang, Efthimios Kaxiras, Manuel Richter, and Jeroen van den Brink, *Creating Weyl Nodes and Controlling Their Energy by Magnetization Rotation*, arXiv:1903.03179.

[12] Yoshinori Tokura, Kenji Yasuda, and Atsushi Tsukazaki, *Magnetic Topological Insulators*, Nat. Rev. Phys. **1**, 126 (2019).

[13] Xufeng Kou, Yabin Fan, Murong Lang, Pramey Upadhyaya, and Kang L. Wang, *Magnetic Topological Insulators and Quantum Anomalous Hall Effect*, Solid State Commun. **215–216**, 34 (2015).

[14] Tomasz Dietl and Hideo Ohno, *Dilute Ferromagnetic Semiconductors: Physics and Spintronic Structures*, Rev. Mod. Phys. **86**, 187 (2014).

[15] Y. L. Chen, J. G. Analytis, J.-H. Chu, Z. K. Liu, S.-K. Mo, X. L. Qi, H. J. Zhang, D. H. Lu, X. Dai, Z. Fang, S. C. Zhang, I. R. Fisher, Z. Hussain, and Z.-X. Shen, *Experimental Realization of a Three-Dimensional Topological Insulator*, Bi_2Te_3, Science **325**, 178 (2009).

[16] Haijun Zhang, Chao-Xing Liu, Xiao-Liang Qi, Xi Dai, Zhong Fang, and Shou-Cheng Zhang, *Topological Insulators in Bi_2Se_3, Bi_2Te_3 and Sb_2Te_3 with a Single Dirac Cone on the Surface*, Nat. Phys. **5**, 438 (2009).

[17] Ferhat Katmis, Valeria Lauter, Flavio S. Nogueira, Badih A. Assaf, Michelle E. Jamer, Peng Wei, Biswarup Satpati, John W. Freeland, Ilya Eremin, Don Heiman, Pablo Jarillo-Herrero, and Jagadeesh S. Moodera, *A High-Temperature Ferromagnetic Topological Insulating Phase by Proximity Coupling*, Nature (London) **533**, 513 (2016).

[18] Y. S. Hor, P. Roushan, H. Beidenkopf, J. Seo, D. Qu, J. G. Checkelsky, L. A. Wray, D. Hsieh, Y. Xia, S.-Y. Xu, D. Qian, M. Z. Hasan, N. P. Ong, A. Yazdani, and R. J. Cava, *Development of Ferromagnetism in the Doped Topological Insulator $Bi_{2-x}Mn_xTe_3$*, Phys. Rev. B **81**, 195203 (2010).

[19] Toru Hirahara, Sergey V Eremeev, Tetsuroh Shirasawa, Yuma Okuyama, Takayuki Kubo, Ryosuke Nakanishi, Ryota Akiyama, Akari Takayama, Tetsuya Hajiri, Shin-Ichiro Ideta *et al.*, *Large-Gap Magnetic Topological Heterostructure Formed by Subsurface Incorporation of a Ferromagnetic Layer*, Nano Lett. **17**, 3493 (2017).

[20] Joseph A. Hagmann, Xiang Li, Sugata Chowdhury, Si-Ning Dong, Sergei Rouvimov, Sujitra J. Pookpanratana, Kin Man Yu, Tatyana A Orlova, Trudy B. Bolin, Carlo U. Segre *et al.*, *Molecular Beam Epitaxy Growth and Structure of Self-Assembled Bi_2Se_3/Bi_2MnSe_4 Multilayer Heterostructures*, New J. Phys. **19**, 085002 (2017).

[21] Dong Sun Lee, Tae-Hoon Kim, Cheol-Hee Park, Chan-Yeup Chung, Young Soo Lim, Won-Seon Seo, and Hyung-Ho Park, *Crystal Structure, Properties and Nanostructuring of a New Layered Chalcogenide Semiconductor, Bi_2MnTe_4*, Cryst. Eng. Commun. **15**, 5532 (2013).

[22] S. V. Eremeev, M. M. Otrokov, and E. V. Chulkov, *Competing Rhombohedral and Monoclinic Crystal Structures in $MnPn_2Ch_4$ Compounds: An Ab-Initio Study*, J. Alloys Compd. **709**, 172 (2017).

[23] M. Otrokov, I. I. Klimovskikh, H. Bentmann, D. Estyunin, A. Zeugner, Z. S. Aliev, S. Gaß, A. U. B. Wolter, A. V. Koroleva, A. M. Shikin, M. Blanco-Rey, M. Hoffmann, I. P. Rusinov, A. Yu. Vyazovskaya, S. V. Eremeev, Yu. M. Koroteev, V. M. Kuznetsov, F. Freyse, J. Sánchez-Barriga, I. R. Amiraslanov, M. B. Babanly, N. T. Mamedov, N. A. Abdullayev, V. N. Zverev, A. Alfonsov, V. Kataev, B. Büchner, E. F. Schwier, S. Kumar, A. Kimura, L. Petaccia, G. Di Santo, R. C. Vidal, S. Schatz, K. Kißner, M. Ünzelmann, C. H. Min, Simon Moser, T. R. F. Peixoto, F. Reinert, A. Ernst, P. M. Echenique, A. Isaeva, E. V. Chulkov, *Prediction and Observation of the First Antiferromagnetic Topological Insulator*, Nature (London) **576**, 416 (2019).

[24] Alexander Zeugner, Frederik Nietschke, Anja U. B. Wolter, Sebastian Gaß, Raphael C. Vidal, Thiago R. F. Peixoto, Darius Pohl, Christine Damm, Axel Lubk, Richard Hentrich, Simon K. Moser, Celso Fornari, Chul Hee Min, Sonja Schatz, Katharina Kißner, Maximilian Ünzelmann, Martin Kaiser, Francesco Scaravaggi, Bernd Rellinghaus, Kornelius Nielsch, Christian Hess, Bernd Büchner, Friedrich Reinert, Hendrik Bentmann, Oliver Oeckler, Thomas Doert, Michael Ruck, and Anna Isaeva, *Chemical Aspects of the Candidate Antiferromagnetic Topological Insulator $MnBi_2Te_4$*, Chem. Mater. **31**, 2795 (2019).

[25] R. C. Vidal, H. Bentmann, T. R. F. Peixoto, A. Zeugner, S. Moser, C.-H. Min, S. Schatz, K. Kißner, M. Ünzelmann, C. I. Fornari, H. B. Vasili, M. Valvidares, K. Sakamoto, D. Mondal, J. Fujii, I. Vobornik, S. Jung, C. Cacho, T. K. Kim, R. J. Koch, C. Jozwiak, A. Bostwick, J. D. Denlinger, E. Rotenberg, J. Buck, M. Hoesch, F. Diekmann, S. Rohlf, M. Kalläne, K. Rossnagel, M. M. Otrokov, E. V. Chulkov, M. Ruck, A. Isaeva, and F. Reinert, *Surface States and Rashba-Type Spin Polarization in Antiferromagnetic $MnBi_2Te_4$(0001)*, Phys. Rev. B **100**, 121104(R) (2019).

[26] Yan Gong, Jingwen Guo, Jiaheng Li, Kejing Zhu, Menghan Liao, Xiaozhi Liu, Qinghua Zhang, Lin Gu, Lin Tang, Xiao Feng, Ding Zhang, Wei Li, Canli Song, Lili Wang, Pu Yu, Xi Chen, Yayu Wang, Hong Yao, Wenhui Duan, Yong Xu, Shou-Cheng Zhang, Xucun Ma, Qi-Kun Xue, and Ke He, *Experimental Realization of an Intrinsic Magnetic Topological Insulator*, Chin. Phys. Lett. **36**, 076801 (2019).

[27] Yang Peng and Yong Xu, *Proximity-Induced Majorana Hinge Modes in Antiferromagnetic Topological Insulators*, Phys. Rev. B **99**, 195431 (2019).

[28] Jiaheng Li, Yang Li, Shiqiao Du, Zun Wang, Bing-Lin Gu, Shou-Cheng Zhang, Ke He, Wenhui Duan, and Yong Xu, *Intrinsic Magnetic Topological Insulators in van der Waals Layered $MnBi_2Te_4$-Family Materials*, Sci. Adv. **5**, eaaw5685 (2019).

[29] Dongqin Zhang, Minji Shi, Tongshuai Zhu, Dingyu Xing, Haijun Zhang, and Jing Wang, *Topological Axion States in the Magnetic Insulator $MnBi_2Te_4$ with the Quantized Magnetoelectric Effect*, Phys. Rev. Lett. **122**, 206401 (2019).

[30] Ziya S. Aliev, Imamaddin R. Amiraslanov, Daria I. Nasonova, Andrei V. Shevelkov, Nadir A. Abdullayev, Zakir A. Jahangirli, Elnur N. Orujlu, Mikhail M. Otrokov, Nazim T. Mamedov, Mahammad B. Babanly, and Evgueni V. Chulkov, *Novel Ternary Layered Manganese Bismuth Tellurides of the $MnTe$-Bi_2Te_3 System: Synthesis and Crystal Structure*, J. Alloys Compd. **789**, 443 (2019).

[31] Daniel Souchay, Markus Nentwig, Daniel Günther, Simon Keilholz, Johannes de Boor, Alexander Zeugner, Anna Isaeva, Michael Ruck, Anja U. B. Wolter, Bernd Büchner, and Oliver Oeckler, *Layered Manganese Bismuth Tellurides with $GeBi_4Te_7$- and $GeBi_6Te_{10}$-type Structures: Towards Multifunctional Materials*, J. Mater. Chem. C **7**, 9939 (2019).

[32] See Supplemental Material at http://link.aps.org/supplemental/10.1103/PhysRevX.9.041065 for Notes 1–7, Figs. S1–S13, and Tables S1–S4.

[33] L. E. Shelimova, O. G. Karpinskii, M. A. Kretova, and G. U. Lubman, *A Physicochemical Investigation of the Layered Semiconducting Compounds $Ge_3Bi_2Te_6$, $GeBi_2Te_4$ and $GeBi_4Te_7$*, Inorg. Mater. (USSR) **29**, 56 (1993).

[34] Stephen Lee, Ernest Fischer, Jeff Czerniak, and N. Nagasundaram, *Synthesis and Structure of Two Phases with Both Extended and Point Defects:* $Mn_{1-x}Bi_{2+y}S_4$ *and* $Mn_{1-x}Bi_{2+y}Se_4$, J. Alloys Compd. **197,** 1 (1993).

[35] Kulugammana G. S. Ranmohotti, Honore Djieutedjeu, and Pierre F. P. Poudeu, *Chemical Manipulation of Magnetic Ordering in* $Mn_{1-x}Sn_xBi_2Se_4$ *Solid-Solutions*, J. Am. Chem. Soc. **134,** 14033 (2012).

[36] C. Hess, A. Kondrat, A. Narduzzo, J. E. Hamann-Borrero, R. Klingeler, J. Werner, G. Behr, and B. Büchner, *The Intrinsic Electronic Phase Diagram of Iron-Oxypnictide Superconductors*, Europhys. Lett. **87,** 17005 (2009).

[37] Jiazhen Wu, Fucai Liu, Masato Sasase, Koichiro Ienaga, Yukiko Obata, Ryu Yukawa, Koji Horiba, Hiroshi Kumigashira, Satoshi Okuma, Takeshi Inoshita, and Hideo Hosono, *Natural van der Waals Heterostructural Single Crystals with Both Magnetic and Topological Properties*, Sci. Adv. **5,** eaax9989 (2019).

[38] M. Z. Shi, B. Lei, C. S. Zhu, D. H. Ma, J. H. Cui, Z. L. Sun, J. J. Ying, and X. H. Chen, *Magnetic and Transport Properties in the Magnetic Topological Insulators* $MnBi_2Te_4(Bi_2Te_3)_n$ *(n = 1, 2)*, Phys. Rev. B **100,** 155144 (2019).

[39] I. I. Klimovskikh, M. M. Otrokov, D. Estyunin, S. V. Eremeev, S. O. Filnov, A. Koroleva, E. Shevchenko, V. Voroshnin, I. P. Rusinov, M. Blanco-Rey *et al.*, *Variety of Magnetic Topological Phases in the* $(MnBi_2Te_4)(Bi_2Te_3)_m$ *Family*, arXiv:1910.11653.

[40] E. A. Turov, *Physical Properties of Magnetically Ordered Crystals* (Academic Press, New York, London, 1965).

[41] Michael Farle, *Ferromagnetic Resonance of Ultrathin Metallic Layers*, Rep. Prog. Phys. **61,** 755 (1998).

[42] M. Abbate, J. B. Goedkoop, F. M. F. de Groot, M. Grioni, J. C. Fuggle, S. Hofmann, H. Petersen, and M. Sacchi, *Probing Depth of Soft X-Ray Absorption Spectroscopy Measured in Total-Electron-Yield Mode*, Surf. Interface Anal. **18,** 65 (1992).

[43] Tom Rauch, Markus Flieger, Jürgen Henk, Ingrid Mertig, and Arthur Ernst, *Dual Topological Character of Chalcogenides: Theory for* Bi_2Te_3, Phys. Rev. Lett. **112,** 016802 (2014).

[44] Roger S. K. Mong, Andrew M. Essin, and Joel E. Moore, *Antiferromagnetic Topological Insulators*, Phys. Rev. B **81,** 245209 (2010).

[45] A. Herdt, L. Plucinski, G. Bihlmayer, G. Mussler, S. Döring, J. Krumrain, D. Grützmacher, S. Blügel, and C. M. Schneider, *Spin-Polarization Limit in* Bi_2Te_3 *Dirac Cone Studied by Angle- and Spin-Resolved Photoemission Experiments and Ab Initio Calculations*, Phys. Rev. B **87,** 035127 (2013).

[46] Chaoyu Chen, Shaolong He, Hongming Weng, Wentao Zhang, Lin Zhao, Haiyun Liu, Xiaowen Jia, Daixiang Mou, Shanyu Liu, Junfeng He, Yingying Peng, Ya Feng, Zhuojin Xie, Guodong Liu, Xiaoli Dong, Jun Zhang, Xiaoyang Wang, Qinjun Peng, Zhimin Wang, Shenjin Zhang, Feng Yang, Chuangtian Chen, Zuyan Xu, Xi Dai, Zhong Fang, and X. J. Zhou, *Robustness of Topological Order and Formation of Quantum Well States in Topological Insula-*

[47] Marco Bianchi, Dandan Guan, Shining Bao, Jianli Mi, Bo Brummerstedt Iversen, Philip D. C. King, and Philip Hofmann, *Coexistence of the Topological State and a Two-Dimensional Electron Gas on the Surface of* Bi_2Se_3, Nat. Commun. **1,** 128 (2010).

[48] Y. L. Chen, J.-H. Chu, J. G. Analytis, Z. K. Liu, K. Igarashi, H.-H. Kuo, X. L. Qi, S. K. Mo, R. G. Moore, D. H. Lu, M. Hashimoto, T. Sasagawa, S. C. Zhang, I. R. Fisher, Z. Hussain, and Z. X. Shen, *Massive Dirac Fermion on the Surface of a Magnetically Doped Topological Insulator*, Science **329,** 659 (2010).

[49] J. Sánchez-Barriga, A. Varykhalov, G. Springholz, H. Steiner, R. Kirchschlager, G. Bauer, O. Caha, E. Schierle, E. Weschke, A. A. Ünal, S. Valencia, M. Dunst, J. Braun, H. Ebert, J. Minár, E. Golias, L. V. Yashina, A. Ney, V. Holý, and O. Rader, *Nonmagnetic Band Gap at the Dirac Point of the Magnetic Topological Insulator* $(Bi_{1-x}Mn_x)Se_3$, Nat. Commun. **7,** 10559 (2016).

[50] Kyle N Gordon, Hongyi Sun, Chaowei Hu, A Garrison Linn, Haoxiang Li, Yuntian Liu, Pengfei Liu, Scott Mackey, Qihang Liu, Ni Ni *et al.*, *Strongly Gapped Topological Surface States on Protected Surfaces of Antiferromagnetic* $MnBi_4Te_7$ *and* $MnBi_6Te_{10}$, arXiv:1910.13943.

[51] Chaowei Hu, Xiaoqing Zhou, Pengfei Liu, Jinyu Liu, Peipei Hao, Eve Emmanouilidou, Hongyi Sun, Yuntian Liu, Harlan Brawer, Arthur P Ramirez *et al.*, *A van der Waals Antiferromagnetic Topological Insulator with Weak Interlayer Magnetic Coupling*, arXiv:1905.02154.

[52] Yong Hu, Lixuan Xu, Mengzhu Shi, Aiyun Luo, Shuting Peng, Z. Y. Wang, J. J. Ying, T. Wu, Z. K. Liu, C. F. Zhang *et al.*, *Universal Gapless Dirac Cone and Tunable Topological States in* $(MnBi_2Te_4)_m(Bi_2Te_3)_n$ *Heterostructures*, arXiv:1910.11323.

[53] L. X. Xu, Y. H. Mao, H. Y. Wang, J. H. Li, Y. J. Chen, Y. Y. Y. Xia, Y. W. Li, J. Zhang, H. J. Zheng, K. Huang *et al.*, *Persistent Gapless Surface States in* $MnBi_2Te_4/Bi_2Te_3$ *Superlattice Antiferromagnetic Topological Insulator*, arXiv:1910.11014.

[54] Hang Li, Shun-Ye Gao, Shao-Feng Duan, Yuan-Feng Xu, Ke-Jia Zhu, Shang-Jie Tian, Jia-Cheng Gao, Wen-Hui Fan, Zhi-Cheng Rao, Jie-Rui Huang, Jia-Jun Li, Da-Yu Yan, Zheng-Tai Liu, Wan-Ling Liu, Yao-Bo Huang, Yu-Liang Li, Yi Liu, Guo-Bin Zhang, Peng Zhang, Takeshi Kondo, Shik Shin, He-Chang Lei, You-Guo Shi, Wen-Tao Zhang, Hong-Ming Weng, Tian Qian, and Hong Ding, *Dirac Surface States in Intrinsic Magnetic Topological Insulators* $EuSn_2As_2$ *and* $MnBi_{2n}Te_{3n+1}$, Phys. Rev. X **9,** 041039 (2019).

[55] Chang Liu, Yongchao Wang, Hao Li, Yang Wu, Yaoxin Li, Jiaheng Li, Ke He, Yong Xu, Jinsong Zhang, and Yayu Wang, *Quantum Phase Transition from Axion Insulator to Chern Insulator in* $MnBi_2Te_4$, arXiv:1905.00715.

[56] Y. Deng *et al.*, *Magnetic-Field-Induced Quantized Anomalous Hall Effect in Intrinsic Magnetic Topological Insulator* $MnBi_2Te_4$, arXiv:1904.11468.

[57] X-Shape, *Crystal Optimization for Numerical Absorption Correction Program, v. 2.12.2, Stoe and Cie GmbH, Darmstadt,* 2009.

[58] V. Petricek, M. Dusek, and L. Palatinus, *JANA2006, The Crystallographic Computing System* (Institute of Physics, Praha, Czech Republic, 2011).

[59] G. M. Sheldrick, *A Short History of SHELX*, Acta Crystallogr. Sect. A **64,** 112 (2008).

[60] Further details on the crystal structure investigations of $Mn_{0.75(3)}Bi_{4.17(3)}Te_7$ can be obtained from the Fachinformationszentrum Karlsruhe, 76344 Eggenstein-Leopoldshafen, Germany [fax, (+49)7247-808-666; email, crysdata@fiz-karlsruhe.de], on quoting the depository number CSD-1891486.

[61] K. Brandenburg, DIAMOND *3.2k,* (Crystal Impact GbR, Bonn, 2014).

[62] A. Barla, J. Nicolás, D. Cocco, S. M. Valvidares, J. Herrero-Martín, P. Gargiani, J. Moldes, C. Ruget, E. Pellegrin, and S. Ferrer, J. Synchrotron Radiat. **23,** 1507 (2016).

[63] John P. Perdew, Kieron Burke, and Matthias Ernzerhof, *Generalized Gradient Approximation Made Simple*, Phys. Rev. Lett. **77,** 3865 (1996).

[64] Klaus Koepernik and Helmut Eschrig, *Full-Potential Nonorthogonal Local-Orbital Minimum-Basis Band-Structure Scheme*, Phys. Rev. B **59,** 1743 (1999), https://www.fplo.de/.

[65] Jorge I. Facio, Sanjib Kumar Das, Yang Zhang, Klaus Koepernik, Jeroen van den Brink, and Ion Cosma Fulga, *Dual Topology in Jacutingaite* Pt_2HgSe_3, Phys. Rev. Mater. **3,** 074202 (2019).